Modeling the Effects of a Light Bridge on Properties of Magnetohydrodynamic Waves in Solar Pores

Luiz A. C. A. Schiavo[1] , Mykola Gordovskyy[2] , Philippa K. Browning[3] , Suzana de Souza e Almeida Silva[4] , Gary Verth[5] ,
Istvan Ballai[5] , Sergiy Shelyag[6] , Sergey N. Ruzheinikov[4] , James A. McLaughlin[1] , and Viktor Fedun[4]
[1] Department of Mathematics, Physics and Electrical Engineering, Northumbria University, Newcastle NE1 8ST, UK
[2] Centre for Astrophysics Research, Department of Physics, Astronomy & Mathematics, University of Hertfordshire, Hatfield AL10 9AB, UK
[3] Jodrell Bank Centre for Astrophysics, University of Manchester, Manchester M13 9PL, UK
[4] Plasma Dynamics Group, School of Electrical and Electronic Engineering, The University of Sheffield, Mappin Street, Sheffield, S1 3JD, UK
[5] Plasma Dynamics Group, School of Mathematical and Physical Sciences, The University of Sheffield, Hounsfield Road, Sheffield, S3 7RH, UK
[6] College of Science and Engineering, Flinders University, Tonsley, SA 5042, Australia
Received 2024 July 8; revised 2024 August 29; accepted 2024 September 9; published 2024 October 24

Abstract

Solar pores are ideal magnetic structures for wave propagation and transport of energy radially outwards across the upper layers of the solar atmosphere. We aim to model the excitation and propagation of magnetohydrodynamic waves in a pore with a light bridge modeled as two interacting magnetic flux tubes separated by a thin, weaker-field layer. We solve the three-dimensional magnetohydrodynamic equations numerically and calculate the circulation as a measure of net torsional motion. We find that the interaction between flux tubes results in the natural excitation of propagating torsional Alfvén waves but find no torsional waves in the model with a single flux tube. The torsional Alfvén waves propagate with wave speeds matching the local Alfvén speed where wave amplitude peaks.

1. Introduction

The structuring of the magnetic field in the solar atmosphere in the form of flux tubes (pores, sunspots, fibrils, prominences, spicules, coronal loops, etc.) provides an ideal environment for mass and energy transfer between different regions permeated by the magnetic field. These structures are also ideal environments for wave propagation and the transport of energy to the upper layers of the atmosphere. The most prominent manifestations of magnetic structures in the solar photosphere are sunspots and pores, locations of the magnetic flux emergence from the solar interior; the differentiation between them resides in the existence of the penumbra region in the case of sunspots. In addition to the difference in their appearances, these two magnetic structures also differ in their size, lifetime, and the average intensity of the magnetic field. While in the darkest parts of the umbra, the magnetic field is of the order of 1.7–3.7 kG (W. Livingston 2002; S. K. Solanki 2003), and in pores, the magnetic field attains values of about 0.6–1.8 kG (G. W. Simon & N. O. Weiss 1970; S. K. Solanki 2003).

Solar pores are intermediate structures between small-scale magnetic flux concentrations in intergranular lanes and fully developed sunspots with penumbrae (R. H. Cameron et al. 2011). This makes them an ideal laboratory for studying wave excitation and propagation, including the dissipation of magnetoacoustic wave energy (S. D. T. Grant et al. 2015; C. A. Gilchrist-Millar et al. 2021), and Alfvén waves (R. J. Morton et al. 2011). These waves traverse upwards through the layers of the lower solar atmosphere along the pore's length, which serve as conduits for magnetohydrodynamic (MHD) waves (R. J. Morton et al. 2011). Moreover, magnetic pores act as waveguides, transmitting significant wave energy to the upper atmosphere and thereby influencing the dynamics and energetics of the lower solar atmosphere (P. H. Keys et al. 2018). Observational evidence has revealed MHD oscillations within solar pores, discernible in line-of-sight velocities, intensities, and magnetic field strengths (C. J. Nelson et al. 2021).

Some sunspots and pores exhibit light bridges—relatively bright elongated structures cutting across a sunspot's or pore's umbra (see Figure 1, left panel, for an example). Observations reveal that light bridges may have a very versatile magnetic structure, which depends on the overall magnetic structure and evolution of the active region. A light bridge can be formed as a result of two magnetic elements coming together during the sunspot evolution, leaving a region with a lower vertical magnetic field at the boundary between the two elements, with the force balance in the light bridge maintained by enhanced (compared to sunspot umbra) gas pressure (see, e.g., J. M. Borrero & K. Ichimoto 2011; T. Felipe et al. 2016; J. Jing et al. 2023, and references therein). Light bridges appear to possess a predominantly vertical magnetic field although the magnetic field strengths in light bridges appear to be significantly lower compared to the umbrae and, in some cases, may be significantly inclined (see, e.g., T. Felipe et al. 2016). In some cases, there might be an overlying magnetic field forming a magnetic canopy or a fibril elongated above a light bridge (e.g., S. Toriumi et al. 2015). The magnetic field in light bridges is very inhomogeneous, and, in some cases, light bridges may have locations with an extremely strong magnetic field (5–10 kG), i.e., much stronger than in umbrae, although with significantly lower filling factors (∼0.25 compared to ∼1 in umbrae, e.g., J. S. Castellanos Durán et al. 2020; V. Lozitsky et al. 2022).

Light bridges in pores have similar characteristics to those in sunspots: their field is mainly vertical although more inclined than in umbrae, and the force balance is maintained by increased gas pressure (M. Sobotka et al. 2013a; R. Kamlah et al. 2023).
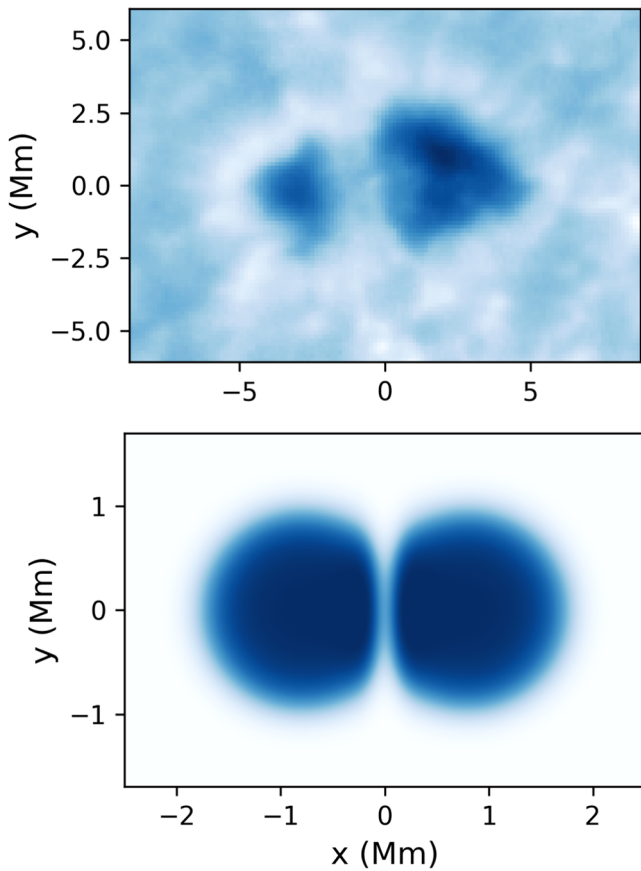
Figure 1. Comparison between an observed pore with a light bridge and the light bridge numerical model. Upper panel shows continuum intensity for a pore with a light bridge in active region AR11005 analyzed by M. Stangalini et al. (2021a). This pore was observed on 2008 October 15, at 16:30 UT at 25.2 N, 10.0 with the Interferometric Bidimensional Spectrometer at the Dunn Solar Telescope (New Mexico, USA). The lower panel presents brightness distributions in our light bridge model.

Hence, in the first approximation, the pores with light bridges can be considered as two intense magnetic flux tubes joined together.

One notable characteristic of light bridges is the enhanced power of chromospheric oscillations typically observed in the frequency range of 3–5 mHz (M. Sobotka et al. 2013b). Recently M. Stangalini et al. (2021a) detected torsional Alfvén waves in an Fe I spectral line in a pore under the presence of a light bridge. They further emphasized the importance of torsional Alfvén waves for chromospheric and coronal heating estimating their energy flux. M. Stangalini et al. (2021a) also performed a numerical simulation of a flux tube driven by a kink driver to generate torsional waves. However, they considered a single tube model for their numerical simulations, which is not consistent with the observed magnetic configuration of a solar pore with a light bridge.

In this work, a photospheric pore with a light bridge is modeled numerically as two closely adjacent magnetic tubes, which represent magnetic elements with a thin layer of weaker magnetic field and higher pressure separating them (see Figure 1). For the analysis of the wave propagation, and in order to focus on the essential physics of waves driven by the presence of the light bridge configuration compared with a single pore, we neglect gravitational stratification and the large-scale velocity field; therefore, our initial configuration is independent of height for simplicity. Although the employed

model is relatively simple, the configuration adequately reflects the main properties of a sunspot or a photospheric pore with a light bridge. Individual oscillating flux tubes driven by kink drivers have already been studied by J. Terradas et al. (2008a), D. J. Pascoe et al. (2010), and P. Antolin et al. (2014).

An attempt to model a realistic situation in the solar atmosphere was to consider magnetic flux tubes as being built up from a multiple of cylindrical structures that show collective motion. Earlier studies by, e.g., J. Terradas et al. (2008b), L. Ofman (2009), D. Robertson & M. S. Ruderman (2011), R. Soler & M. Luna (2015), N. Magyar & T. Van Doorsselaere (2016), and M. Shi et al. (2024), showed that in such systems the interaction between individual structures modifies the spatial structures and morphology of waves. Here, for the first time, we are simulating two closely adjacent magnetic elements forming a light bridge under kink motion.

2. Numerical Simulations

2.1. Main Equations

We perform three-dimensional ideal MHD simulations of oscillations in a model representing a pore and a pore with the light bridge using the Lare3D code where MHD equations are solved in the Lagrangian form employing a Lagrangian–Eulerian remap procedure (T. D. Arber et al. 2001). The equations solved by Lare3D are presented in dimensionless form as

$$\frac{D\rho}{Dt} = -\rho \nabla \cdot \boldsymbol{v}, \tag{1}$$

$$\rho \frac{D\boldsymbol{v}}{Dt} = (\nabla \times \boldsymbol{B}) \times \boldsymbol{B} - \nabla p + f_{\text{visc}}, \tag{2}$$

$$\frac{D\boldsymbol{B}}{Dt} = (\boldsymbol{B} \cdot \nabla)\boldsymbol{v} - \boldsymbol{B}(\nabla \cdot \boldsymbol{v}), \tag{3}$$

$$\frac{D\epsilon}{Dt} = -\frac{p}{\rho} \nabla \cdot \boldsymbol{v}, \tag{4}$$

$$p = \rho \epsilon (\gamma - 1), \tag{5}$$

where $\boldsymbol{v}$ denotes the velocity vector, $\boldsymbol{B}$ represents the magnetic field, ρ indicates plasma density, p corresponds to gas pressure, ϵ is the specific internal energy, and γ is the ratio of specific heats, here set to $5/3$. To address numerical instabilities and manage steep gradients, such as shocks, a numerical viscosity vector, f_{visc}, is introduced (E. J. Caramana et al. 1998; T. D. Arber et al. 2001).

The model assumes a fully ionized plasma, and the governing equations are normalized by a length-scale L_0, magnetic field strength B_0, and density ρ_0. These three constants are further utilized to establish normalization for velocity $(v_0 = B_0/\sqrt{\mu_0 \rho})$, pressure $(p_0 = B_0^2/\mu_0)$, time $(t_0 = L_0/v_0)$, specific internal energy scales $(\epsilon_0 = v_0^2)$, and temperature $(T_0 = \epsilon_0 \bar{m}/k_B)$, where μ_0 is the vacuum permeability, k_B is the Boltzmann constant, and $\bar{m}$ is the average ion mass, defined as 1.2 times the proton mass. While the simulation results can be scaled with any suitable reference scales, they are defined here to align with typical values of the photosphere, specifically $L_0 = 1$ Mm, $B_0 = 0.17$ T, and $\rho_0 = 1.67 \times 10^{-4}$ kg m^{-3}. Therefore, the normalization velocity and temperature are $v_0 = 11.7$ km s^{-1} and $T_0 = 20,000$ K, respectively, and the scale time is $t_0 = 85$ s.

In our simulations, the normalized computational domain box size is $8 \times 6 \times 16$ in the x-, y-, and z-directions, respectively. The simulation box is extended in the z-direction
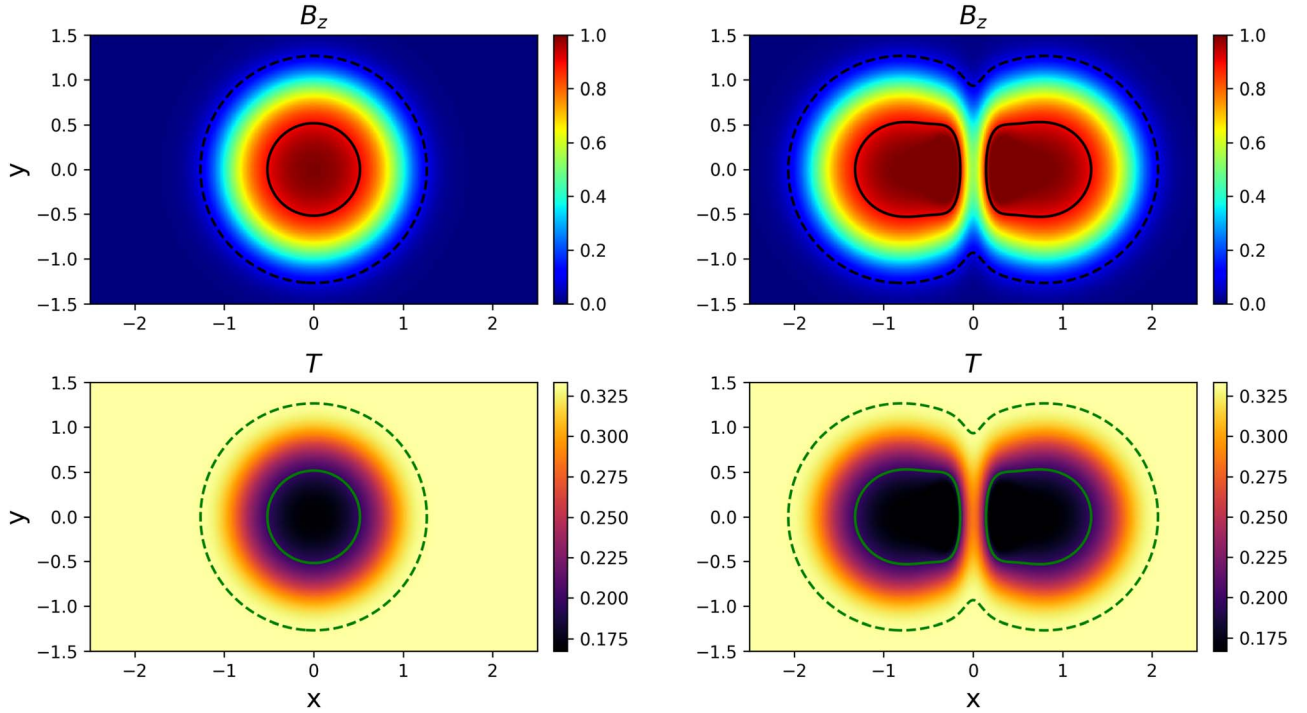
Figure 2. The initial conditions for the magnetic field, B_z, and the continuum intensity for the single flux tube model (left panels) and the light bridge model (right panels). Dashed lines and solid lines represent isocontours of $B_z = 0.1$ and $B_z = 0.9$. The upper panels show contours of z-component of the magnetic field. The lower panels show contours of temperature, where the normalizing scales are $B_0 = 0.17$ T and $T_0 = 20,000$ K.

to 16 to minimize the effect of wave reflections from the upper boundary. However, our analysis only considers the domain between $z = 0$ and $z = 8$. Each considered model covers a time period that was over 150 Alfvén times.

2.2. Initial and Boundary Conditions

We consider two models: a "reference" configuration with a single, cylindrical magnetic flux tube and one with two partially merged flux tubes with magnetic field depression between them. The latter configuration is used to simulate a photospheric pore with a light bridge.

The initial magnetic field and temperature for these configurations are shown in Figure 2.

The inhomogeneous initial magnetic field in the single flux tube model is given as a two-dimensional Gaussian function centered on the origin

$$B(x, y) = B_0 \exp\left(-\frac{x^2 + y^2}{R_0^2}\right), \tag{6}$$

while in the case of the light bridge model, the magnetic field is given as

$$B(x, y) = B_0\left[\exp\left(-\frac{(x - x_s)^2 + y^2}{R_0^2}\right) + \exp\left(-\frac{(x + x_s)^2 + y^2}{R_0^2}\right) - \exp\left(-\frac{32x^2 + y^2}{R_0^2}\right)\right]. \tag{7}$$

The latter term in this equation is used to create a magnetic field depression between the two partially merged flux tubes.

This region, with the magnetic field strength lower and the temperature higher than inside the flux tubes, represents the light bridge (see the right panels in Figure 2). Here $R_0 = 1.0L_0$ is the flux tube radius. The parameter x_s, which determines the relative positions of the flux tubes in the light bridge model, is taken to be $0.8L_0$. The initial density is assumed to be constant $\rho(x, y, z, t = 0) = \rho_0$, while the pressure distribution is obtained, assuming the magnetohydrostatic equilibrium condition:

$$\rho(x, y, z, t = 0) = \rho_0, \tag{8}$$

$$p(x, y, z, t = 0) = p_0 - \frac{B^2(x, y, z, t = 0)}{2\mu_0}, \tag{9}$$

$$\epsilon(x, y, z, t = 0) = \frac{p(x, y, z, t = 0)}{\rho_0(\gamma - 1)}. \tag{10}$$

The ambient pressure value is set to $p_0 = B_0^2/\mu_0$. Hence, the gas pressure and temperature inside the flux tubes is ~2 times lower than outside.

The left panels show the magnetic configuration with a single flux tube, while the right panels correspond to the magnetic configuration with two partially overlapping flux tubes, with the overlap region with magnetic field depression representing the light bridge. The solid lines in Figure 2 correspond to isocontours of $B_z = 0.9$, effectively representing the cores of the flux tubes.

Periodic boundary conditions are used at the side boundaries of the model domains ($x = -4$, $x = 4$, $y = -3$, and $y = 3$). At the upper boundary of the numerical domain, we use Neumann boundary conditions, setting a zero gradient for every variable. At the lower boundary ($z = 0$), the same zero gradient conditions are imposed on all variables apart from v_y. The v_y

component of the velocity, which is used as a driver, is given as

$$v_y(x, y, z = 0, t) = A \sin\left(\frac{2\pi}{\lambda}t\right)g(x, y), \qquad (11)$$

where A denotes the driver amplitude that was set at a value of 0.05 to guarantee v_y perturbations stay in the linear regime, and the function $g(x, y)$ is set as

$$g(x, y) = 0.5\left[1 + \tanh\left(\frac{R_d - \sqrt{\frac{x^2}{4} + y^2}}{0.2}\right)\right]. \qquad (12)$$

This function is a constant equal to 1 in the middle of the lower boundary, in a region with the radius $R_d = 1.5$, and reduces to 0 near the side boundaries. Therefore, the bases of the flux tubes in both models oscillate in the y-direction as one whole, while there, the driver's velocity is 0 at the edges of the lower boundary.

The quantity λ represents the oscillation period or the period of the driver (chosen as $10t_0$, equal to 850 s, corresponding to the frequency of 1.2 mHz).

3. Results

3.1. Flow Evolution

Before analyzing the behavior of the flux tubes, we will examine the evolution of vorticity and magnetic field lines over an oscillation cycle. Figure 3 illustrates the z-component of the vorticity field, $\omega_z = (\nabla \times \boldsymbol{v})_z$, and velocity vectors at four successive simulation time steps within an oscillation period for the cases of a single flux tube (left column) and light bridge simulations (right column). As before, the dashed and continuous lines represent the isocontours of the vertical component of the magnetic field, B_z, set at 0.1 and 0.9, respectively.

The vorticity is prominently observed in a boundary layer outside the core of the flux tube, extending to its external boundary. This vorticity generation seems to be associated with the kinking motion of the flux tube core. In the case of the single flux tube, two symmetric vortices are observed at $x = \pm 0.8$ and $y = 0$, while in the light bridge case, there are four vortices along the x-axis. Despite this difference, the vorticity profiles remain symmetric, albeit with a higher amplitude in the case of a sunspot with a light bridge. Periodic changes in the rotational patterns between clockwise and counterclockwise directions characterize the small swirling motions observed at $y = 0$ along the x-axis. These periodic changes in swirl orientation create a wave pattern in the vorticity contour, which is visible at the edges of the flux tubes. This vorticity oscillation generates a periodic torsional motion that can be associated with a torsional Alfvén wave. The field lines in the flux tube core exhibit a kink mode behavior characterized by a near-zero B_x component, indicative of minimal vortical motion.

Figure 4 illustrates the outcomes of a power spectral density (PSD) analysis conducted for v_z at $z = 4$. The contour plots depict the PSD results for each grid point at the driver frequency, $f_D = 1/\lambda$. As usual, the maximum of PSD corresponds to regions where the power of waves takes its maximum value. To avoid the initial transient, these PSDs were computed using time-series data collected from $t = 20$ to $t = 100$.

The PSD contour maps for a single flux tube show a strong signal for v_z between the flux tube core and its boundary, indicating wave propagation. The light bridge case displays a similar pattern, but we can see that the interaction between flux tubes creates an intense signal in the light bridge.

The light bridge case shows a prominent signal between the boundary and the pore core. However, this signal diminishes toward the middle of the light bridge, a finding consistent with those reported by M. Stangalini et al. (2021b), who noted a lack of noticeable amplitude in the velocity line-of-sight PSD at the light bridge in observational data for frequencies of 6 and 8 mHz and no signal from circular polarization.

3.2. Net Circulation

In order to detect the possible existence of azimuthal motions associated with torsional Alfvén waves, we compute the circulation, Γ, for each simulation as a measure of net torsional motion. The circulation, well-known in fluid dynamics, is defined as the line integral of a velocity vector field around a closed curve,

$$\Gamma = \oint_C \boldsymbol{v} \cdot d\boldsymbol{l} = \iint_S \nabla \times \boldsymbol{v} \cdot d\boldsymbol{S} = \iint_S \boldsymbol{\omega} \cdot d\boldsymbol{S}, \qquad (13)$$

where C is the closed curve and S the surface defined by the closed curve C, and $\boldsymbol{\omega} = \nabla \times \boldsymbol{v}$ is the vorticity vector. The circulation integrated over $x - y$ planes for each simulation case is shown in Figure 5 at different time steps. The integrating surface, S, is chosen to be an isocontour of $B_z = 0.7$. The area was chosen to be large enough to capture the vorticity oscillation, while small enough to capture a single lobe of the flux tube. The left column features contour plots of B_z, with the dashed–dotted line indicating the integration area set to correspond to $B_z = 0.7$, and the dashed and continuous lines represent the flux tube boundary and its core. The right column presents the normalized circulation by the driver amplitude, A. The upper row corresponds to the single flux tube simulation, while the lower row represents the light bridge simulation.

As indicated by the upper right panel, the net circulation is negligible in the single flux tube, as expected due to the antisymmetry of the z vorticity contours shown in Figure 3. Between $t = 0$ and $t = 40$, the net circulation remains very close to zero. This is expected from the azimuthal symmetry of this configuration as there is no preferred direction for net torsional circulation. However, after this period, some low-amplitude waves are observed being reflected from the upper boundary toward the bottom of the domain. Fortunately, these waves do not compromise the analysis since their amplitude is 10 times smaller than the driver amplitude. By contrast, in the light bridge case, the net circulation for a single tube is (in each lobe of the light bridge) no longer zero. In this case, the normalized circulation exhibits an amplitude 3 times larger than the driver perturbation and propagates as a wave toward the upper boundary at $z = 8$. This suggests an upward-propagating torsional Alfvén mode with a single frequency and constant velocity. This arises from the interaction between the two lobes in the light bridge simulation and leads to
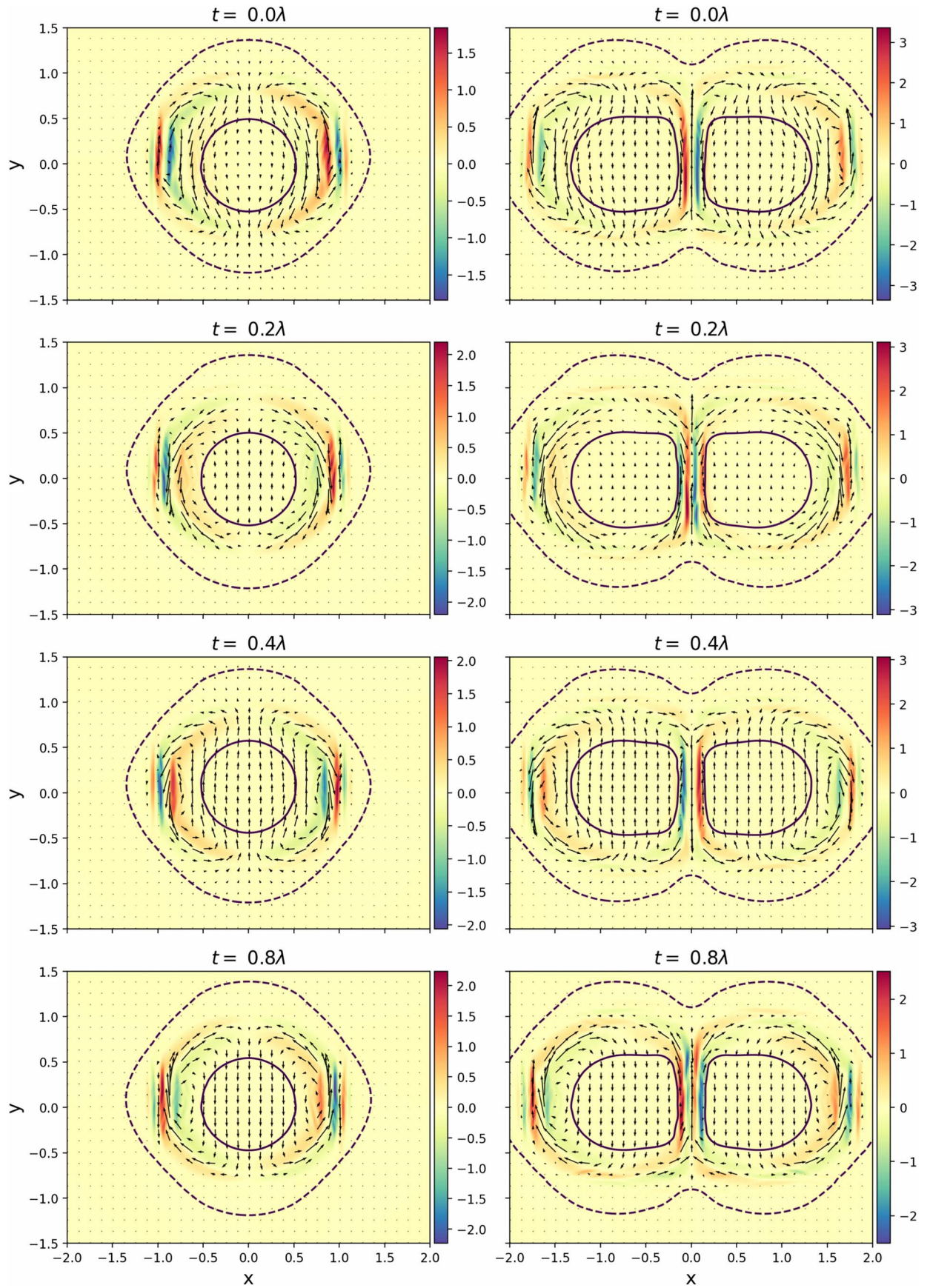
Figure 3. Contours of z-component of vorticity measured at $z = 8$. The arrows represent the velocity vector at different simulation times. The left panels represent the single tube simulation, while the right panels represent the light bridge model. λ represents the period of perturbation.
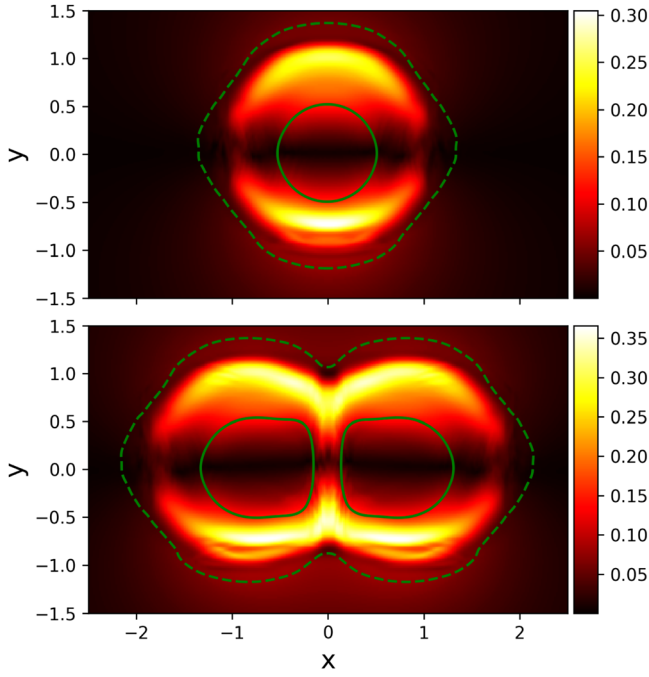
Figure 4. Contours of PSD of v_z measured at $z = 4$ at the diver frequency; upper panel displays results for a single flux tube, and the lower panel displays results for the light bridge model. The light bridge case presents a higher power between the pore core and the boundary.

an asymmetry in each lobe's vorticity profile, resulting in a net circulation. Equivalently, the azimuthal symmetry in each lobe is broken due to the distortion from the light bridge, allowing net torsional circulation to develop. The waves reflected in the light bridge case are not visible on the spacetime diagram because they have a small amplitude. The influence of reflected waves can be disregarded in this analysis as their amplitude is more than 10 times smaller than that of the upward-propagating wave.

Figure 6 displays the results of the PSD computed for the space-time diagram presented in Figure 5, specifically for the light bridge case. The PSD computation involves spatial analysis in the z-direction between $t = 40$ and 140, followed by averaging to determine the dominant wavenumber. We selected this particular time interval to keep the analysis free from the influence of initial transients. Temporal PSD is then calculated between $z = 3$ and 8 to mitigate upper and lower boundary effects; the result was also averaged to smooth the signal. The main frequency and the primary wavenumber were identified and used to compute a phase speed of 0.531 v_0, corresponding to 11.6 km s^{-1}. The right panel of Figure 6 shows the values of ω_z for $z = 8$ at $t = 50$. The black dashed–dotted lines indicate locations where the propagation speed equals the local value of the Alfvén speed. Notably, the phase speed matches the Alfvén speed within the outer boundary layer of the flux tube and more or less in the location where the vorticity peaks in magnitude, so the wave amplitude is strongest. This suggests a torsional Alfvén wave localized within this layer.

3.3. MHD Modes

In order to analyze the nature of perturbations in the system, we employ the wave decomposition method described in detail by S. Mumford et al. (2015). In the context of linear

perturbations in a uniform homogeneous magnetized plasma, the ideal MHD equations have three independent eigenmodes corresponding to the fast and slow magnetoacoustic waves and the Alfvén waves. These modes exhibit distinct properties, with characteristics dependent on the plasma conditions in which the waves propagate. Decomposing perturbations into these modes is a nontrivial problem.

Identifying the three modes of oscillation in a 3D geometry becomes feasible in the presence of flux tubes. The fast, slow, and Alfvén modes can be associated with velocity perturbations perpendicular to the magnetic field and the flux tube, perturbations parallel to the flux tube and its surface, and an azimuthal vector perpendicular to the magnetic field and parallel to the surface, respectively. S. Mumford et al. (2015) proposed the following decomposition for the energy flux:

$$F_\parallel = \rho v_\parallel^2 c_S, \tag{14}$$

$$F_\perp = \rho v_\perp^2 v_A, \tag{15}$$

$$F_\theta = \rho v_\theta^2 v_A, \tag{16}$$

where $F_\parallel$, $F_\perp$, and F_θ are the parallel, perpendicular, and azimuthal components of the energy flux; $v_\parallel$, $v_\perp$, and v_θ are the parallel, perpendicular and azimuthal velocity components; and c_S, v_A are the sound and Alfvén speeds. The azimuthal component computed by $\boldsymbol{n}_\theta = \boldsymbol{n}_\perp \times \boldsymbol{n}_\parallel$, where $\boldsymbol{n}_\parallel$ is the unit vector parallel to the magnetic field and $\boldsymbol{n}_\perp$ is perpendicular to the surface constructed numerically within a computational domain as an isosurface where $|\boldsymbol{B}| = 0.8$. Given the assumption that perturbations are small, we consider the isosurface to be parallel to the magnetic field lines. This 3D surface allows us to obtain the vectors $\boldsymbol{n}_\theta$ and $\boldsymbol{n}_\perp$. In Figure 7, we present the velocity field decomposed into parallel ($v_\parallel$), perpendicular ($v_\perp$), and azimuthal (v_θ) components. Notably, the perpendicular velocity component exhibits a larger amplitude near the driver and decays along the z-direction, while the azimuthal and parallel components demonstrate similar amplitudes along the z-direction.

In Figure 8, we show the energy flux decomposition based on Equations (14)–(16). The kink driver induces a peak in the perpendicular energy flux component, $F_\perp$, near the bottom of the domain, which propagates upwards and attenuates rapidly. The component $F_\parallel$ has its minimum at $z = 0$ and increases with z. In the absence of any dissipative effect, it is likely that $F_\perp$ is being converted into $F_\parallel$ as it propagates to higher altitudes. The azimuthal energy flux, F_θ, is generated at the lower boundary by the kink driver, with an apparent intensification around $z = 7$. The driver contributes to both perpendicular and azimuthal perturbations, which means torsional waves and kink waves; such behavior has also been observed by S. Mumford et al. (2015) and M. Stangalini et al. (2021a). In our model, plasma β is less than 1, which means that the $F_\parallel$, $F_\perp$, and F_θ are associated with the dominant eigenfunctions representing a slow magnetoacoustic, fast magnetoacoustic, and Alfvén waves, respectively (D. B. Jess et al. 2015). Therefore, since θ is the azimuthal component, F_θ will be associated with the energy flux of a torsional Alfvén wave.
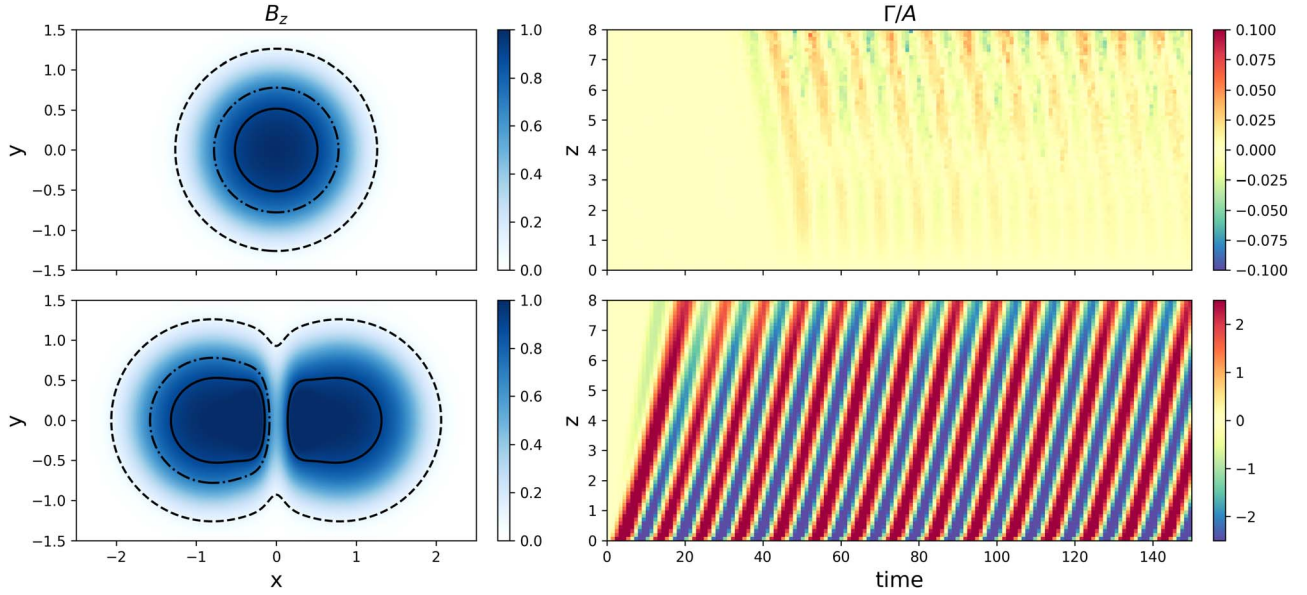
Figure 5. The upper row shows results for the single flux tube simulation, and the bottom row show results for the light bridge simulation. Left panels: contour plots of B_z. The dashed–dotted line delimits the path of integration employed to compute circulation, the dashed line represents $B_z = 0.1$, and the solid line represents $B_z = 0.9$. Right panels: time-distance diagram of the circulation normalized by the driver amplitude, A.
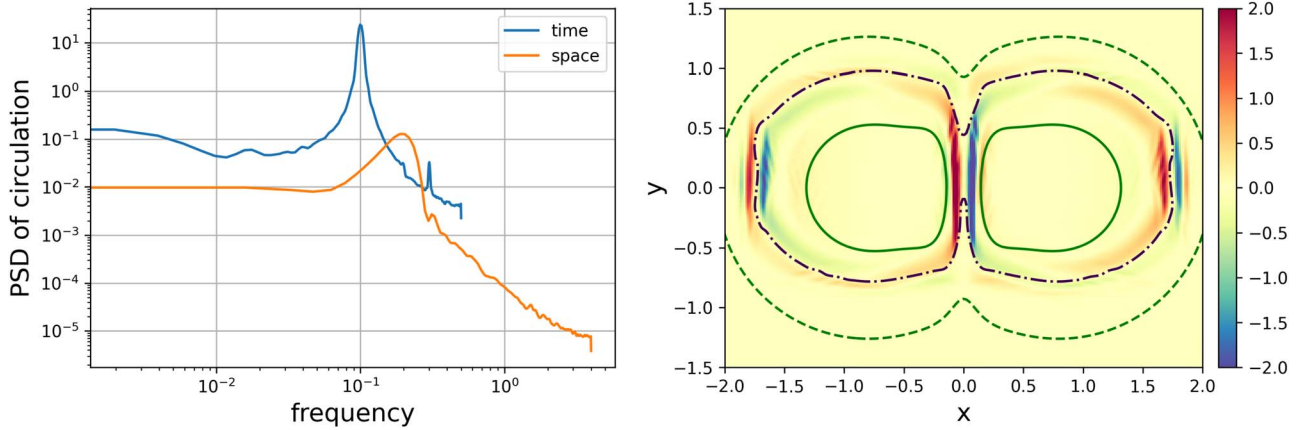
Figure 6. Left panel: PSD applied to circulation in space and time. Right panel: plot of ω_z for $z = 8$ at $t = 50$. The black dashed–dotted line indicates the region where wave speed is equal to Alfvén speed. Green dashed line and solid lines represent isocontours of $B_z = 0.1$ and $B_z = 0.9$, respectively.

4. Conclusions

Our investigation focused on a pore with a light bridge, which we modeled as two closely adjacent magnetic flux tubes separated by a thin layer of weaker field. To simplify our analysis and in order to focus on generic properties of wave propagation and generation, we ignored gravitational stratification and large-scale velocity fields, which allowed us to generate a height-independent initial configuration. Despite this simplification, our model effectively captures the primary characteristics of a sunspot or a photospheric pore with a light bridge, both driven by a kink driver at their bases.

An examination of vorticity and field line evolution revealed that no vorticity is generated within the flux tube core, where the axial field is 90% or more than its peak value ($B_z > 0.9$), and the field lines exhibit kink body-wave motions. Vorticity emerges between the pore core and its boundary, with the light bridge scenario demonstrating intensified vorticity near the light bridge. Vorticity profiles no longer exhibit symmetry within each lobe, in contrast to what is observed in a single flux tube.

In the case of a single flux tube, the net circulation remains minimal due to a cancellation between vorticity profiles of opposite sign on either side of the tube, resulting from symmetry across the y-axis. However, the presence of two closely adjacent flux tubes disrupts this balance, leading to a net circulation of significant magnitude in each lobe of the light bridge. This disruption causes torsional motion on each side due to their interaction, with torsional waves occurring in the boundary layer between the edges of the flux tubes and their cores. Notably, we found that the speed of these waves matches the local Alfvén speed in regions where wave amplitude peaks.

Our analysis of the MHD mode decomposition elucidates that the kink driver engenders both torsional and kink waves. Moreover, the perpendicular energy flux to the flux tube surface decreases with height while the azimuthal component increases.
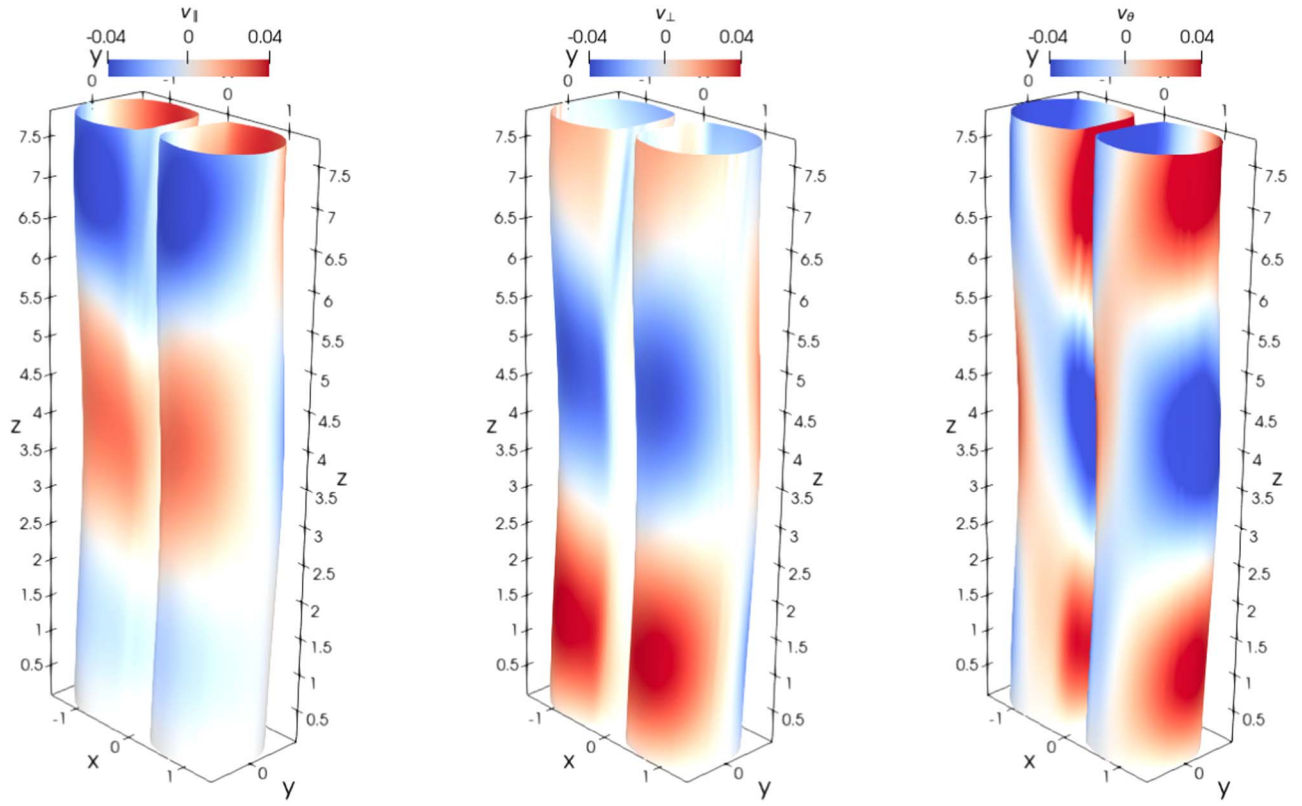
Figure 7. Contours of velocity field decomposed into parallel, $v_\parallel$; perpendicular, $v_\perp$; and azimuthal, v_θ, components.
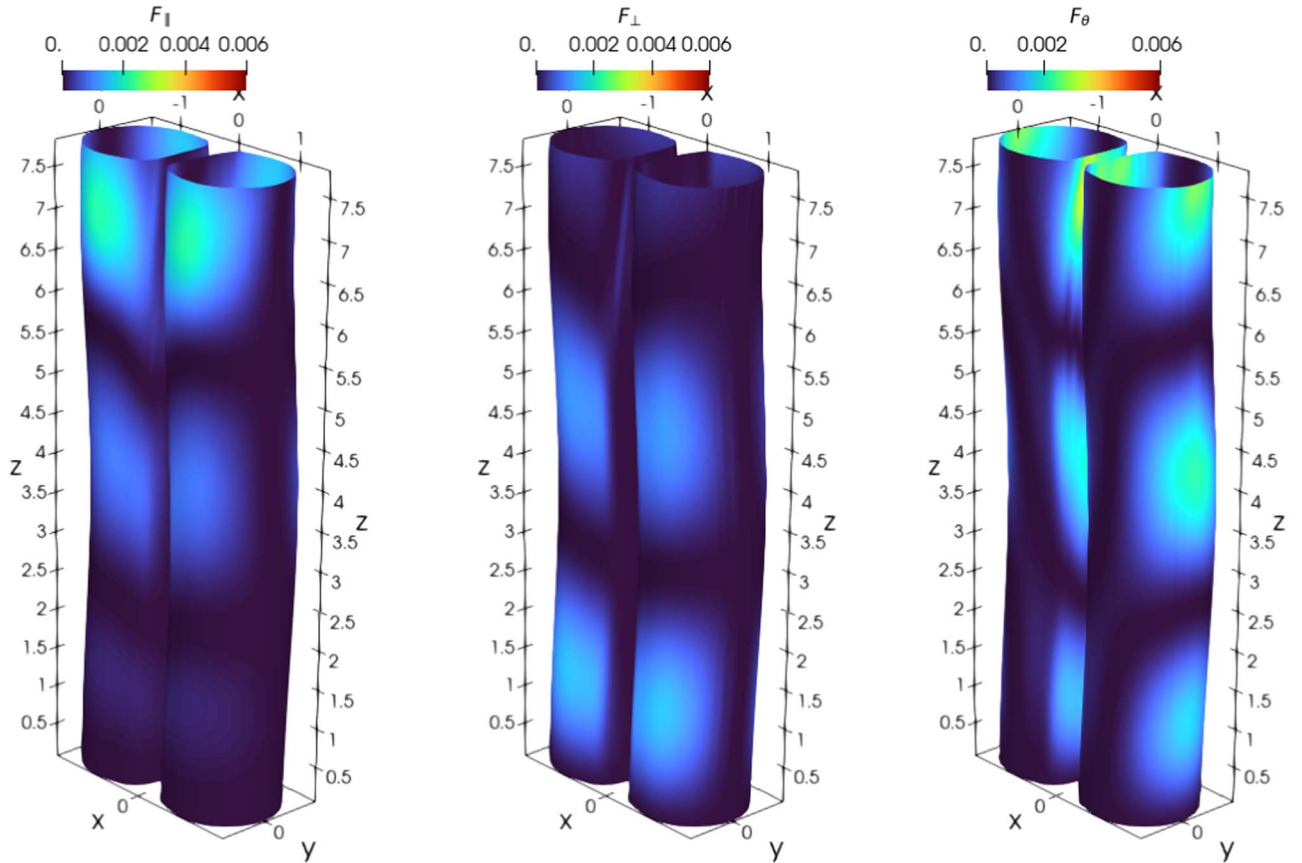
Figure 8. Contours of energy flux field decomposed into parallel, $F_\parallel$; perpendicular, $F_\perp$; and azimuthal, F_θ, components.

Importantly, we demonstrated that a single flux tube driven by a kink driver does not exhibit net torsional motion, a result that contradicts the numerical modeling reported by M. Stangalini et al. (2021a). Our model establishes a new and crucial understanding: net torsional motion arises from the interaction between the two lobes of the pore and that including this structuring in the background model is essential for interpreting waves observed in pores and sunspots with light bridges.

ORCID iDs

Luiz A. C. A. Schiavo https://orcid.org/0000-0002-5082-1398
Mykola Gordovskyy https://orcid.org/0000-0003-2291-4922
Philippa K. Browning https://orcid.org/0000-0002-7089-5562
Suzana de Souza e Almeida Silva https://orcid.org/0000-0001-5414-0197
Gary Verth https://orcid.org/0000-0002-9546-2368
Istvan Ballai https://orcid.org/0000-0002-3066-7653
Sergiy Shelyag https://orcid.org/0000-0002-6436-9347
Sergey N. Ruzheinikov https://orcid.org/0000-0002-3219-5004
James A. McLaughlin https://orcid.org/0000-0002-7863-624X
Viktor Fedun https://orcid.org/0000-0002-0893-7346

References

Antolin, P., Yokoyama, T., & Van Doorsselaere, T. 2014, ApJL, 787, L22
Arber, T. D., Longbottom, A. W., Gerrard, C. L., & Milne, A. M. 2001, JCoPh, 171, 151
Borrero, J. M., & Ichimoto, K. 2011, LRSP, 8, 4
Cameron, R. H., Vögler, A., & Schüßler, M. 2011, A&A, 533, A86
Caramana, E. J., Shashkov, M. J., & Whalen, P. P. 1998, JCoPh, 144, 70
Castellanos Durán, J. S., Lagg, A., Solanki, S. K., & van Noort, M. 2020, ApJ, 895, 129
Felipe, T., Collados, M., Khomenko, E., et al. 2016, A&A, 596, A59
Gilchrist-Millar, C. A., Jess, D. B., T. Grant, S. D., et al. 2021, RSPTA, 379, 20200172
Grant, S. D. T., Jess, D. B., Moreels, M. G., et al. 2015, ApJ, 806, 132
Jess, D. B., Morton, R. J., Verth, G., et al. 2015, SSRv, 190, 103
Jing, J., Liu, N., Lee, J., et al. 2023, ApJ, 952, 40
Kamlah, R., Verma, M., Denker, C., & Wang, H. 2023, A&A, 675, A182
Keys, P. H., Morton, R. J., Jess, D. B., et al. 2018, ApJ, 857, 28
Livingston, W. 2002, SoPh, 207, 41
Lozitsky, V., Yurchyshyn, V., Ahn, K., & Wang, H. 2022, ApJ, 928, 41
Magyar, N., & Van Doorsselaere, T. 2016, ApJ, 823, 82
Morton, R. J., Erdélyi, R., Jess, D. B., & Mathioudakis, M. 2011, ApJL, 729, L18
Mumford, S., Fedun, V., & Erdélyi, R. 2015, A&A, 799, 6
Nelson, C. J., Campbell, R. J., & Mathioudakis, M. 2021, A&A, 654, A50
Ofman, L. 2009, ApJ, 694, 502
Pascoe, D. J., Wright, A. N., & De Moortel, I. 2010, ApJ, 711, 990
Robertson, D., & Ruderman, M. S. 2011, A&A, 525, A4
Shi, M., Li, B., Chen, S., Yu, H., & Guo, M. 2024, A&A, 686, A2
Simon, G. W., & Weiss, N. O. 1970, SoPh, 13, 85
Sobotka, M., Švanda, M., Jurčák, J., et al. 2013a, A&A, 560, A84
Sobotka, M., Švanda, M., Jurčák, J., Heinzel, P., & Del Moro, D. 2013b, JPhCS, 440, 012049
Solanki, S. K. 2003, A&ARv, 11, 153
Soler, R., & Luna, M. 2015, A&A, 582, A120
Stangalini, M., Erdélyi, R., Boocock, C., et al. 2021a, NatAs, 5, 691
Stangalini, M., Jess, D. B., Verth, G., et al. 2021b, A&A, 649, A169
Terradas, J., Andries, J., Goossens, M., et al. 2008a, ApJ, 687, L115
Terradas, J., Arregui, I., Oliver, R., et al. 2008b, ApJ, 679, 1611
Toriumi, S., Katsukawa, Y., & Cheung, M. C. M. 2015, ApJ, 811, 137